

Chapter 2

Theoretical Considerations

2.1 Metal optics

The propagation of light inside a metal is characterized by scattering processes. In the visible-light region the scattering is due to excitations in the conduction band. In the x-ray range the optical properties are governed by the presence of absorption edges, where also the index of refraction (i.e. the light velocity inside the medium) undergoes characteristic changes with the wave length. This behavior can be understood within the classical oscillator model. To give an appropriate description of the physics at an absorption edge, one would conceive as many oscillators as there are possible optical transitions. However, an exact description in the frame of quantum mechanics is not essentially different from a simple description which – for a fundamental understanding – can be provided by classical arguments, and to which the present discussion shall be restricted.

Each bound electron in an atom shall now be represented by an isotropic linear oscillator acting under the influence of the alternating electro-magnetic field of the incoming light. With the restriction that the wavelength of the incident light is much larger than the oscillator, the equation of motion of the electron is that of a damped forced oscillator,

$$m\ddot{\vec{r}} = -m\omega_0^2\vec{r} - \gamma m\dot{\vec{r}} + e\vec{E}_0 e^{i\omega t}. \quad (2.1)$$

Here m is the electron mass, ω_0 the oscillator eigenfrequency, γ the damping-constant¹, and $\vec{E}_0 e^{i\omega t}$ the plane wave of the incoming light with frequency ω . Introducing the solution $\vec{r} = \vec{r}_0 e^{i\omega t}$ in eq. 2.1 one obtains a relation between the electric field of the light wave and the motion of the electron:

$$\vec{r} = \frac{e/m}{\omega_0^2 - \omega^2 + i\gamma\omega} \vec{E}. \quad (2.2)$$

The proportionality factor between \vec{r} and \vec{E} is complex, i.e. it includes a phase shift between \vec{E} and the electron motion. In describing an ensemble of N oscillators one defines

¹The damping characterizes the energy loss of the oscillator as the wave is reemitted.

the polarization \vec{P} inside the medium as a macroscopic response to the exciting electromagnetic wave:

$$\vec{P} = \sum_s N_s e \vec{r}_s = \left[\sum_s \frac{N_s e^2 / m}{\omega_s^2 - \omega^2 + i \gamma_s \omega} \right] \vec{E} = \alpha \vec{E}, \quad (2.3)$$

The proportionality factor α between \vec{P} and \vec{E} is the polarizability. It is expressed by the commonly used dielectric tensor ϵ (ϵ_0 in vacuum) defined through the electric displacement \vec{D} (in units SI) by

$$\vec{D} = \epsilon_0 \epsilon \vec{E} = \epsilon_0 \vec{E} + \vec{P} = \epsilon_0 \vec{E} (1 + \alpha / \epsilon_0). \quad (2.4)$$

ϵ is generally complex. It can be separated into real and imaginary part

$$\epsilon = \epsilon' - i \epsilon'', \quad (2.5)$$

where ϵ' characterizes the dispersive, and ϵ'' the absorptive behavior of the medium.

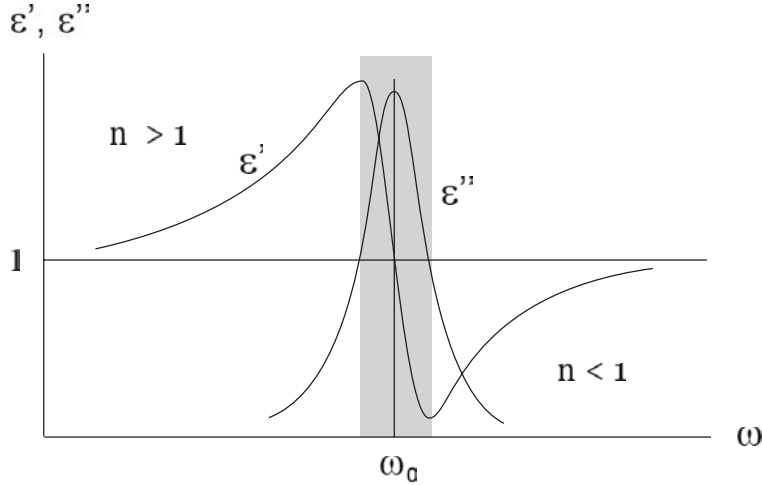


Figure 2.1. Real (ϵ') and imaginary (ϵ'') part of the complex dielectric constant for a single oscillator, characterizing *dispersive* and *absorptive* behavior, respectively. The grey shaded area assigns the region where the real part of the refractive index behaves 'anomalous'.

For a single oscillator the real and imaginary parts of the complex dielectric constant are shown in Fig. 2.1. The *absorption* has a sharp peak at the transition energy $\hbar\omega_0$, i.e. it is important only in the vicinity of the resonance (even unique, since the dispersion has a zero crossing). In going off-resonance, the *dispersion* decays much slower and dominates over the absorption; in this region the refractive index is usually $n \approx 1 - \delta$ [43]. For a single oscillator, the real part of n is smaller than unity below resonance ($\omega < \omega_0$) but larger than unity above ($\omega > \omega_0$).

In the x-ray region, where the individual atoms in a solid can be assumed to scatter the incoming light independently, the process of light propagation may be described by atomic scattering factors f . This is a good assumption for photon energies above about 50 eV [34]. The scattering factor f is defined as the ratio of the amplitude of a wave scattered at an atom, to the amplitude of a wave scattered at a free electron. In the frame of the oscillator model, a description of the scattering at a free electron is obtained by modifying

the oscillator-equation (eq.2.2) such that $\omega_0 = 0$ and $\gamma = 0$ [44]. One obtains for the scattering factor of a single dipole oscillator with the eigenfrequency ω_0 , excited by a wave with frequency ω :

$$f(\omega) = \frac{-\omega^2}{\omega_0^2 - \omega^2 + i\gamma\omega}. \quad (2.6)$$

The enhancement of the scattering factor arising from a multi-electron atom is obtained by summing over all single oscillators which contribute to the process of scattering. Depending on the position of the observer, the spatial distribution of these oscillators within the atom lead to a phase variation due to the individual pathlength from each electron. This variation of the phase provides an angular dependence of the scattering factor:

$$f(\Delta k, \omega) = \sum_{s=1}^Z \frac{-\omega^2 e^{-i\Delta k \cdot \Delta r_s}}{\omega_s^2 - \omega^2 + i\gamma_s \omega}. \quad (2.7)$$

The calculation of the angular-dependent scattering is rather tedious, however, in the dipole approximation (long-wave limit: $a_0 \ll \lambda$, $\Delta k \cdot \Delta r_s \ll 1$) and/or at small scattering angles the expression reduces to the *atomic forward scattering factor*,

$$f^0(\omega) = \sum_{s=1}^Z \frac{-\omega^2}{\omega_s^2 - \omega^2 + i\gamma_s \omega}, \quad (2.8)$$

of which the numerical values can be found in tables [34]. Usually the scattering factor is written in terms of the dispersive real part and absorptive imaginary part:

$$f^0(\omega) = f_1^0(\omega) - i f_2^0(\omega). \quad (2.9)$$

The scattering factor is directly related to the dielectric constant by

$$\epsilon = 1 - \frac{n_a e^2 / m}{\epsilon_0 \omega^2} f^0(\omega), \quad (2.10)$$

where n_a is the electron density per unit volume. Similarly, by use of $n^2 = \epsilon$, one may argue in terms of the optical constants. In the visible-light and soft-x-ray region the complex index of refraction can be written as

$$n = 1 - \delta + i\beta, \quad (2.11)$$

so the real (f_1) and imaginary part (f_2) of the scattering factor are related to the optical constants δ and β in a simple way (this expression is actually an approximation, since it is obtained by linearizing the square root):

$$\delta = \frac{n_a e^2 / m}{2\epsilon_0 \omega^2} f_1^0(\omega) \quad (2.12)$$

$$\beta = \frac{n_a e^2 / m}{2\epsilon_0 \omega^2} f_2^0(\omega). \quad (2.13)$$

For many physical problems, including the damped oscillator, the *Kramers-Kronig transformation* (KKT) relates the real and imaginary parts of a complex function [34,43,44]. In fact the KKT is nothing but an application of *Cauchy's residue theorem* to an analytical complex function. The knowledge of the imaginary part permits one to determine the corresponding real part by integration over the complex plane. Applied to the formalism of light scattering, the following dispersion relations are commonly used in order to determine the imaginary part of the atomic scattering factor $f_2^0(\omega)$ from absorption measurements, and calculate the corresponding real part $f_1^0(\omega)$:

$$f_2^0(\omega) = \frac{\epsilon_0 m^2 \omega c}{e^2 \rho} \mu(\omega) \quad (2.14)$$

$$f_1^0(\omega) = Z^* - \frac{2}{\pi} \mathcal{P} \int_0^\infty \frac{u^2 f_2^0 du}{u^2 - \omega^2}, \quad (2.15)$$

where Z is the atomic number and \mathcal{P} indicates the non-diverging principle part of the integral. The essential point of this relation is that each point in $f_1^0(\omega)$ requires an integration over the whole frequency range of $f_2^0(\omega)$, although the integral in eq. 2.15 is only important in the vicinity of the transition frequency ω_0 and, as we will see below (section 5.3), it is not necessary to integrate up to infinity². In the limit of very high photon energies, f_1^0 approaches the atomic number Z (for high- Z elements $Z \rightarrow Z^*$, including relativistic corrections). Values for f_1 and f_2 are tabulated for a large energy range and can be found in Ref. [34].

2.2 Magneto Optics

The magneto-optical (MO) Kerr effect describes the propagation of light in a medium under the influence of a magnetic induction \vec{B} . In order to obtain a basic understanding of these MO effects one may once again use the single-oscillator model.

In the presence of a magnetic field the moving electron is subject to the Lorentz force. It acts normal to the propagation direction of the electron, giving rise to a rotation of the plane of polarization. The motion of the electron under the influence of an magnetic field can be described by extending the fundamental equation of motion by the Lorentz-term,

$$m\vec{r} = -m\omega_0^2\vec{r} - \gamma m\dot{\vec{r}} + e(\vec{E} + \vec{v} \times \vec{B}), \quad (2.16)$$

where \vec{v} is the velocity of the electron.

The electric field \vec{E} of the light wave and the induced electric displacement \vec{D} inside the medium are related by the frequency-dependent dielectric tensor $\epsilon(\omega)$, of which the off-diagonal elements describe the magnetic field-induced rotation. In an isotropic (cubic) system the dielectric tensor can be written

²The necessary range of integration depends on the f_2 -function and changes with the edge considered.

$$\vec{D} = \epsilon_0 \epsilon \vec{E} - i \epsilon_0 \epsilon Q \vec{\sigma} \times \vec{E} = \epsilon_0 \epsilon \begin{pmatrix} 1 & iQ\sigma_3 & -iQ\sigma_2 \\ -iQ\sigma_3 & 1 & iQ\sigma_1 \\ iQ\sigma_2 & -iQ\sigma_1 & 1 \end{pmatrix} \vec{E}, \quad (2.17)$$

where Q is a material dependent constant, and the σ_i 's are the components of the reduced magnetization ($i = 1, 2, 3$)³. In the non-magnetic state (e.g. $T > T_C$) the off-diagonal elements are zero, and there are no magnetization-induced changes in the polarization of the propagating light. In case of a magnetic field or long-range magnetic order, the Lorentz force induces a component normal to the directions of primary movement (\vec{E}) and magnetization ($\vec{\sigma}$), which changes the polarization of the propagating wave.

In a sufficiently transparent medium one can study the light transmitted through the sample (Faraday effect). The change in polarization arises from the fact that the refractive index (propagation velocity, and absorption) is different for left and right circularly polarized light⁴.

Linearly polarized light can be understood as a superposition of left and right circularly polarized light. In the transmitted light the two phase-shifted components recombine to form a linearly polarized beam of rotated polarization. The rotation is proportional to the magnetization of the medium, as it is expressed by the *Verdet constant* V

$$\Delta\Phi = \frac{\omega d}{2c}(n_+ - n_-) = VdH, \quad (2.18)$$

n_{\mp} is the index of refraction for left and right circularly polarized light, respectively, and d is the thickness of the sample. This equation states that the difference in the index of refraction for left and right helicity is proportional to the thickness of the sample and to the magnetic field H .

In reflection (Kerr effect) the situation is considerably more complicated since one has to describe the light vector inside the medium by use of the *Fresnel equations*. In reflection the characteristic length is the penetration depth of light. In a quantum mechanical picture the MO effects are related to modifications of the energy levels by a magnetic field (*Zeeman effect*).

There are three different MOKE geometries which, according to their relative orientation of magnetization, light polarization, and plane of incidence, are known as *polar*, *longitudinal*, and *transversal* Kerr-effect. In the polar geometry the magnetization is oriented normal to the sample surface. The effect is strongest for normal incidence, and independent of polarization. If the magnetization is parallel to the sample surface, one distinguishes between the two possible orientations with respect to the plane of incidence: parallel in the longitudinal geometry and normal in the transverse geometry. For all geometries one may say that the rotation of polarization is proportional to the component of magnetization parallel to the light beam. From the fact that the MO Kerr effect is linear in magnetization, one can see that the rotation is inverted upon reversal of magnetization.

³The reduced magnetization is defined as $\sigma := M(T)/M(0)$.

⁴Circular polarized light is a macroscopic expression for an ensemble of photons with the same helicity, i.e. carrying the same spin.

2.3 Magnetic x-ray absorption

According to Beer's law the intensity of a photon beam decays exponentially as it penetrates a homogeneous piece of matter:

$$I(d) = I_0 \cdot e^{-\mu(\omega) \cdot d}, \quad (2.19)$$

with μ being the linear absorption coefficient and d the thickness of the sample. In the x-ray region the energy dependence of μ is $\sim \omega^{-7/2}$ (this holds strictly only for K shells [45]) and shows characteristic jumps ('absorption edges') at photon energies which equal the electron binding energies of the atomic shells, i.e. the absorption edges are element specific (law of Mosley). They are called K -, L_I , L_{II} , L_{III} , ... if an electron is excited from a $1s$ -, $2s$ -, $2p_{1/2}$ -, $2p_{3/2}$ -, ... shell.

For magnetic systems the absorption can depend on the light polarization and on the magnetization. Such a magnetization dependent absorption can be obtained by reversing either the polarization or the magnetization. In case of circularly polarized light the absorption coefficient depends on the relative orientation of helicity and magnetization, denoted μ^+ for parallel and μ^- for antiparallel orientation. The difference between μ^+ and μ^- is known as 'magnetic dichroism', a term that is commonly used in the x-ray region. Through magnetic dichroism we gain information on the magnetic state of a sample by means of spectroscopy. Its principle is the same as for the Zeeman effect, and the suggestion came up to call it inverse Zeeman effect [46].

To obtain a basic understanding of magnetic dichroism we can use a single-electron model. In the vicinity of an absorption threshold, the absorption coefficient μ is given by the product of the transition probability to excite an electron from an occupied initial state $|i\rangle$ into an unoccupied final state $|f\rangle$, and the density of empty states above the Fermi level $\rho_f(\omega)$ (*Fermi's golden rule*), i.e.

$$\mu(\omega) = \frac{2\pi}{\hbar} \cdot |\langle f | \vec{A} \cdot \vec{p} | i \rangle|^2 \cdot \rho_f(\omega), \quad (2.20)$$

with the vector potential \vec{A} characterizing the incident radiation field with the electron momentum \vec{p} . As the appearance of higher-order transitions strongly depends on the wavelength λ as compared to the characteristic absorber dimension a (quadrupole terms are proportional to $(\frac{a}{\lambda})^2$, whereas octupole terms are proportional to $(\frac{a}{\lambda})^4$ [47]), it is not necessary to include all kinds of radiation, and in most cases restriction to dipole transitions is a good approximation. In the dipole approximation, $|\vec{A}| \approx \text{const.}$, and using $\vec{A} \approx A \cdot \vec{e}$, the general expression $\vec{A} \cdot \vec{p}$ simplifies to $\vec{e} \cdot \vec{r}$, with \vec{e} describing the photon polarization, and the position operator \vec{r} replacing \vec{p} .

The initial and final states are characterized by their orbital momentum J and magnetic quantum number M , and will be denoted in the following $|JM\rangle$ for the initial and $|J'M'\rangle$ for the final state, respectively:

$$|\langle f | \vec{A} \cdot \vec{p} | i \rangle|^2 \propto |\langle J'M' | \vec{e} \cdot \vec{r} | JM \rangle|^2 \quad (2.21)$$

In spherical coordinates, both \vec{e} and \vec{r} are conveniently expressed by spherical harmonics, allowing a separation into individual transition probabilities for each photon polarization state. In the circular basis this will be helical left, helical right, and linear (equal contribution of both helicities), denoted by the parameter $q = -1, +1, 0$, respectively.

$$|\langle J'M'|e \cdot r|JM\rangle|^2 \propto \sum_q |\langle J'M'|P_q|JM\rangle|^2. \quad (2.22)$$

$P_q = \sqrt{(4/3)\pi r} Y_1^q(\Theta, \phi)$ denotes the corresponding component of the electric-dipole moment, expressed by spherical harmonics. According to the *Wigner-Eckart theorem* [48], the matrix element in eq. 2.22 can be separated into an angular and a radial part:

$$|\langle J'M'|P_q|JM\rangle|^2 = \underbrace{|\langle J'||P||J\rangle|^2}_{\text{radial}} \underbrace{\begin{pmatrix} J & 1 & J' \\ -M & q & M' \end{pmatrix}^2}_{\text{angular}}. \quad (2.23)$$

The radial part gives the line strength; the angular part, denoted by the $3j$ symbol, describes the distribution of the line strength over all transitions $M \rightarrow M'$. For a given light polarization only some transitions are allowed according to the selection rules. The $3j$ -symbol assures that the selection rules are satisfied (first line), i.e. dipole transitions can only occur if $(J \ 1 \ J')$ satisfies the triangle relation

$$\Delta J \equiv J - J' = 0, \pm 1, \quad (2.24)$$

with the restriction that $J = J' = 0$ is not allowed. For the magnetic component and the polarization vector of the light (second line of the $3j$ -symbol) we have

$$-M + q + M' = 0,$$

where q characterizes the light polarization (see above).

In a simple mean-field picture one can conceive magnetic order as a Zeeman-type splitting of the M sublevels. They are separated by the magnetic-dipole energy $g_J \mu_B B_A$ of the total magnetic moment $g_J \mu_B$ in the exchange field B_A ; g_J is the Landé factor of the total momentum J . At temperatures well below the Curie point, $T \ll T_C$, the Zeeman splitting is much larger than the thermal energy kT . In this limit, only the lowest sublevel $M = -J$ is populated, referred to as *the magnetic ground state* $|J, -J\rangle$. At finite temperatures, however, higher sublevels will also be occupied, with a population according to the Boltzmann factor $\exp(-g_J \mu_B B_A/kT)$. The (Boltzmann weighted) average of the population of the M -sublevels, $\langle M \rangle_{kT}$, is proportional to the size of the temperature-dependent magnetization:

$$|M(T)| \propto \langle M \rangle_{kT}. \quad (2.25)$$

The potential of magnetic dichroism to measure the magnetization is based on the fact that the difference of the partial transition probabilities is exactly proportional to $\langle M \rangle_{kT}$:

$$\begin{aligned}
(\mu^+ - \mu^-) = \langle J' || P || J \rangle^2 \cdot & \left(\left(\begin{array}{ccc} J & 1 & J' \\ \langle -M \rangle_{kT} & q & \langle M - 1 \rangle_{kT} \end{array} \right)^2 \right. \\
& \left. - \left(\begin{array}{ccc} J & 1 & J' \\ \langle -M \rangle_{kT} & q & \langle M + 1 \rangle_{kT} \end{array} \right)^2 \right), \tag{2.26}
\end{aligned}$$

and therefore the quantity $(\mu^+ - \mu^-)$ measures the size of the magnetization $|M(T)|$ [49].

Let us take the Gd $4d \rightarrow 4f$ excitation threshold as example of a dichroic dipole transition, here from a $d^{10}f^7$ ground state to a d^9f^8 final state. In the ground state the completely filled d^{10} shell has a total angular momentum and total spin of zero ($L=0, S=0$), the f^7 -state is half-filled and has a vanishing total angular moment ($L=0$) but maximum spin $S=7/2$ (according to Hund's rule). We take d^{10} and f^7 both together, and look at them as if they were one state. Their total angular momentum is $J_{tot} = S_{tot} = 7/2$ ($L_{tot} = 0$) and the $(d^{10}f^7)$ configuration is in a ${}^8S_{7/2}$ state⁵. With circularly polarized light of either left or right helicity ($q = -1$ or $q = +1$), dipole transitions with $(\Delta M = +1, \Delta J = -1)$ or with mainly $(\Delta M = -1, \Delta J = +1)$ are allowed.

The more severe one-particle selection rules for the E1 transitions ($\Delta l = \pm 1, \Delta s = 0$), would only allow the three final state lines ${}^8P_{7/2}$ ($\Delta J=0$), ${}^8P_{9/2}$ ($\Delta J=+1$), and ${}^8P_{5/2}$ ($\Delta J=-1$). However, they are softened by the *4d-spin-orbit coupling* giving rise to additional transitions (e.g. ${}^8D_{9/2}, \Delta L = +2$). Hence, all together there are several dozen of multiplet lines to be considered in lanthanide $4d - 4f$ absorption spectra. It is this rich multiplet structure that gives rise to drastic spectral variations of the magnetic dichroism, as one scans the photon energy across a $4d - 4f$ excitation threshold (see section 5).

2.4 Magnetism in lanthanide metals

2.4.1 Magnetic order

Contrary to the itinerant transition-metal ferromagnets, magnetism in lanthanide metals is dominated by the huge magnetic moments of the $4f$ electrons. They are localized close to the nucleus and give the main contribution to the magnetic moment. The delocalized $5d$ and $6s$ electrons of the outer shells are involved in chemical bonding, and electronic conductivity; at the same time they serve as a carrier of spin information between the non-interacting $4f$ states at different sites of the lattice. Although the conduction band is polarized, its contribution to the total moment is small.

The indirect exchange coupling named after M. A. Rudermann, C. Kittel, T. Kasuya, and K. Yosida (RKKY), is mediated by the $5d$ and $6s$ conduction electrons. It is described by the effective Hamiltonian

$$H = - \sum_{ij} \mathcal{J}_{ij} \vec{S}_i \vec{S}_j, \tag{2.27}$$

⁵Standard notation: ${}^{2S+1}L_J$

where S_i and S_j are the interacting spins at lattice sites i and j . The function \mathcal{J}_{ij} describes the RKKY exchange interaction strength. It is a long-ranging interaction that has an oscillating behavior, and it decays at large distances as $1/r_{ij}^3$.

Let us consider the total angular momentum

$$\vec{J} = \vec{L} + \vec{S}$$

of the $4f$ shell of a RE atom, which usually comprises spin and orbital contributions. In the paramagnetic phase one observes an effective magnetic moment:

$$\mu_{eff} = -g\mu_B\sqrt{J(J+1)}, \quad (2.28)$$

In the ferromagnetic phase the observed magnetic moment slightly differs from the effective moments, because in the ferromagnetic phase the moments include the conduction electron contribution [50]. For Tb (Gd) the effective moment is $\mu_{eff}^{Tb} = 9.72 \mu_B$ ($\mu_{eff}^{Gd} = 7.94 \mu_B$), and the observed moment is $\mu_{obs}^{Tb} = 9.77 \mu_B$ ($\mu_{obs}^{Gd} = 7.98 \mu_B$) [50, 51].

Only the component that is parallel to \vec{J} contributes effectively to the exchange coupling strength [52]. The component parallel to \vec{J} is $(g-1)J$, so that the exchange coupling strength and the ordering temperature follows the de-Gennes factor⁶

$$\mathcal{J}_{ij} \propto (g-1)^2 J(J+1). \quad (2.29)$$

In heavy lanthanide metals (seven or more $4f$ electrons) the de-Gennes factor is related to the (highest) ordering temperature by a $\xi^{2/3}$ -law [52].

Except for Gd all heavy rare-earth (RE) metals reveal an antiferromagnetic phase (AF), which separates the ferromagnetic (FM) and paramagnetic (PM) phases. Below T_N the magnetic moments couple ferromagnetically within the basal plane (\mathcal{J}_{\parallel}). Along the c -axis the coupling between adjacent basal planes is \mathcal{J}_{\perp} . The intralayer coupling \mathcal{J}_{\parallel} is much stronger than the interlayer coupling \mathcal{J}_{\perp} . In a simplified picture, lanthanide magnetism may be discussed by assuming a chain of equally spaced magnetic moments, which represent the single layers [53].

In the case of Tb the magnetisation between adjacent planes is rotated about the c -axis [54]. The driving mechanism arises from the oscillatory RKKY interaction that mediates ferromagnetic coupling between nearest-neighbor planes, and antiferromagnetic coupling between next-nearest-neighbor planes. The interplanar coupling $\mathcal{J}_{\perp}(Q)$ is strongest at a wave number $2\pi/\lambda_{hel} = Q$, which characterizes the helical structure of magnetic moments. In bulk Tb the interlayer angle of rotation is $\sim 20^\circ$. In Gd the $Q = 0$ over the whole temperature range, i.e. Gd is a pure ferromagnet. The elements Tb, Dy, and Ho show helical arrangements; all others rare-earth elements have a more complicated magnetic structure [52, 55, 56].

As reported by many authors during the last years [57–61], the first-order phase transition in Tb metal from AF to FM is smeared out over a considerable temperature range, in which blocks of ferromagnetic units are separated by regions of helical order. With

⁶de-Gennes factor = $(g_J - 1)^2$.

decreasing temperature the ferromagnetic blocks become thicker until (at ~ 180 K) the entire system becomes ferromagnetically aligned [61]. Recent results from neutron-diffraction studies of bulk-like Tb films [61] revealed periodic magnetic structures over a wide temperature range from slightly above T_N , down to several ten Kelvin below T_C (~ 170 K). The structures have been interpreted as arising from ferromagnetic blocks, which occur (at least in parts of the sample) over this wider temperature range around T_C . Similar to the helical layer-by-layer ordering in the AF phase, the magnetization between neighboring blocks is slightly rotated. The block phase in Tb is most stable against external fields in the vicinity of T_C .

The stability of the helix against field-induced ferromagnetic alignment may be expressed by the difference in exchange-interaction $\mathcal{J}(Q) - \mathcal{J}(0)$ between helical ($q = Q$) and ferromagnetic ($q = 0$) order. The critical field H_{crit} , which is necessary to switch from helical order to ferromagnetic alignment, is defined by

$$\mu H_{crit} = J^2 \sigma^2 [\mathcal{J}(Q) - \mathcal{J}(0)]. \quad (2.30)$$

J is the total $4f$ -momentum quantum number ($J = 6$ in the Tb ground state). The temperature dependence is described by multiplying with the reduced (experimental) magnetization σ [51, 53, 62]. At approximately $H_{crit}/2$ occurs a first-order transition to an intermediate state, as the helix switches to a so-called *fan structure* [60, 63]. In the fan structure the angle θ between the moments and the magnetic field is given by [51]

$$\sin \frac{\theta_i}{2} = \left\{ \frac{2g\mu_B(H_{crit} - H)}{J[3\mathcal{J}(Q) - 2\mathcal{J}(0) - \mathcal{J}(2Q)]} \right\}^{1/2} \sin \vec{Q} \vec{R}_i, \quad (2.31)$$

i.e. there is a layer-by-layer oscillation of the direction of the moments about the magnetization, depending on the applied magnetic field H and the exchange interaction. (Note that a *fan structure* is experimentally hard to distinguish from the ferromagnetic alignment). According to eq. (2.30) there are two different physical quantities which determine the temperature dependence of H_{crit} , namely the (reduced) magnetization $\sigma(T)$ and the temperature dependence of $\mathcal{J}(Q) - \mathcal{J}(0)$ [64, 65].

Due to the strong angular dependence of the $4f$ electron wave function the rare-earths can have a significant crystalline anisotropy. The basal-plane anisotropy in hcp Tb metal is 125 K/atom at low temperatures and hereby dominates over all other anisotropy terms. Therefore the magnetic moments may safely be assumed to lie in the basal plane at all temperatures and moderate magnetic fields (up to several kOe) [57]. Hence, during the magnetization reversal the moments are restricted to rotations within the basal plane of the Tb hcp lattice, and thus the only relevant contribution is given by the sixfold anisotropy K_6^6 of the basal plane. With some 0.6 K/atom near 0 K [51, 55] its strength is comparable to laboratory fields only at very low temperatures, and rapidly decreases with increasing temperature (see appendix). The theory of temperature dependent magneto-crystalline anisotropy is mainly due to Callen & Callen [66]. Experimental investigations on Tb bulk anisotropies from low temperature to ~ 200 K can be found in Refs. [57, 67]. It allows one

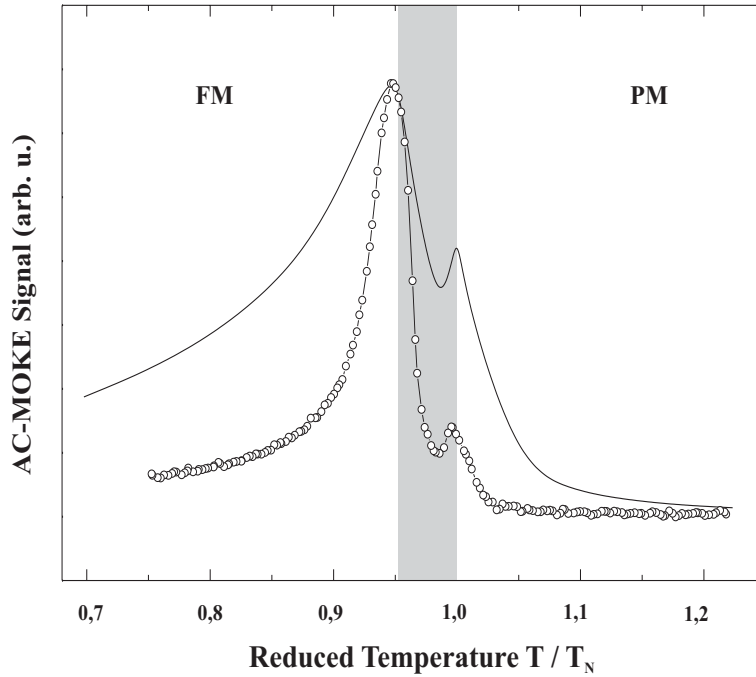


Figure 2.2. Experimental magnetic susceptibility of 10 nm Tb/W(110) at $H_{ext} = 13$ Oe (open symbols). After deposition of the Tb film at room temperature, the sample was annealed at 890 K. The susceptibility peaks at 230 K (T_N) and 219 K (T_C). Susceptibility data from a Tb single crystal at 0.5 Oe internal field are plotted for comparison (solid curve) [del Moral et al., 1974]. The oscillating field is oriented along the b -axis (bulk easy axis) in both cases.

to estimate an upper limit for $K_6^6(T)$ near the transition and ordering temperatures (see also appendix).

The response of the magnetization to an external field - known as the *magnetic susceptibility* - can be written in differential form

$$\chi = \left(\frac{\partial M}{\partial H} \right)_T. \quad (2.32)$$

At temperatures where the system undergoes a magnetic phase transition (PM→AF or AF→FM), both phases are equal in free-energy (the thermodynamic potentials have a crossing point) so that the ordering parameter $M(T)$ can be easily changed by an external field, i.e. the magnetic susceptibility shows a maximum. In the *paramagnetic* region the magnetic susceptibility follows the Curie-Weiss law, $\chi \propto 1/(T - T_N)$, and it diverges at the ordering temperature [68, 69]. In the *helical* region (between T_N and T_C) the susceptibility is lowered by the difference in exchange energy $\mathcal{J}(Q) - \mathcal{J}(0)$ between helical and ferromagnetic order [51, 55, 56]. $\mathcal{J}(Q) - \mathcal{J}(0)$ has a maximum in the helical range [51, 60] lowering the susceptibility to a minimum between T_N and T_C . In the *ferromagnetic* region the susceptibility arises from domain-wall movements and the susceptibility shows an M^2/K -dependence where M is the magnetization and K the crystalline anisotropy [68, 69]. Experimentally the magnetic susceptibility is observed by measuring the response ΔM of the sample to a small oscillating field ΔH .

An experimental example of the magnetic susceptibility versus temperature of a 10-nm Tb film on a W(110) substrate is shown in Fig.2.2 together with data from bulk Tb [70]. One can easily distinguish the two maxima at the magnetic phase transition temperatures

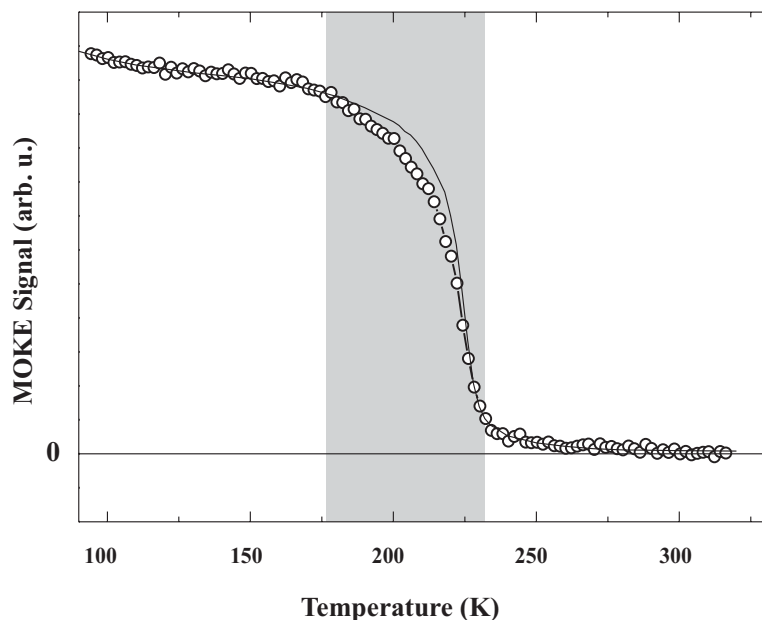


Figure 2.3. Magnetization versus temperature of a 10-nm Tb film on W(110) (open circles) compared with bulk Tb data (solid curve) from [Hegland et al. 1963]. Helical order is expected in the grey shaded temperature range (see text).

T_N and T_C . One observes that the relative signal intensity $i = I_{Curie}/I_{Neel}$ is about 2 times bigger in 10-nm thick Tb film as compared to bulk Tb metal ($i_{bulk} \approx 0.31$, $i_{film} \approx 0.67$), and the peak width is about half as big as in the bulk case.

The magnetic behavior of Tb was first examined by Thoburn et al., using a *polycrystalline sample*. They observed a paramagnetic temperature of 232 K and weak antiferromagnetism between 218 K and 230 K, which could be suppressed by an applied field of ~ 800 Oe [54]. Hegland et al. determined the Néel temperature of a Tb *single crystal* as 229 K [71]. It was found that the phase transition temperatures T_N and T_C sensitively depend on the purity of the sample. This explains why various experiments later on revealed different results ($T_N = 221.7 - 231$ K [72, 73]; $T_C = 210 - 225$ K [73, 74]). However, the most often cited temperatures are $T_N = 230$ K and $T_C = 220$ K [51, 55, 56].

The magnetization of 10-nm Tb/W(110) is depicted in Fig. 2.3 together with data of a Tb single crystal [71]. The applied field is 1 kOe in both cases, which is strong enough to overcome the helical order and align the moments, but still is sufficiently weak to keep the paramagnetic contribution small (above T_N). Just below the ordering temperature the magnetization rises with a steep slope, presumably owing to strong basal-plane anisotropy in Tb (see Fig. 2.3). Note that the magnetic behavior of the thin Tb film deviates significantly from bulk Tb in the temperature range where helical or partial-helical ordering is expected (grey shaded area); see also Appendix.

Magnetic hysteresis loops recorded at 69 K, 196 K, and 217 K in Fig. 2.4 show the field dependence of the Tb film magnetization. The remanent magnetization is about 13% smaller than the magnetization at 1.7 kOe. This is comparable with the behavior of bulk Tb [71], where the saturation moment in the ferromagnetic regime is reached only at fields of ~ 5 kOe [71].

The macroscopic *coercive field* H_C is related to the energy necessary to rotate the Tb

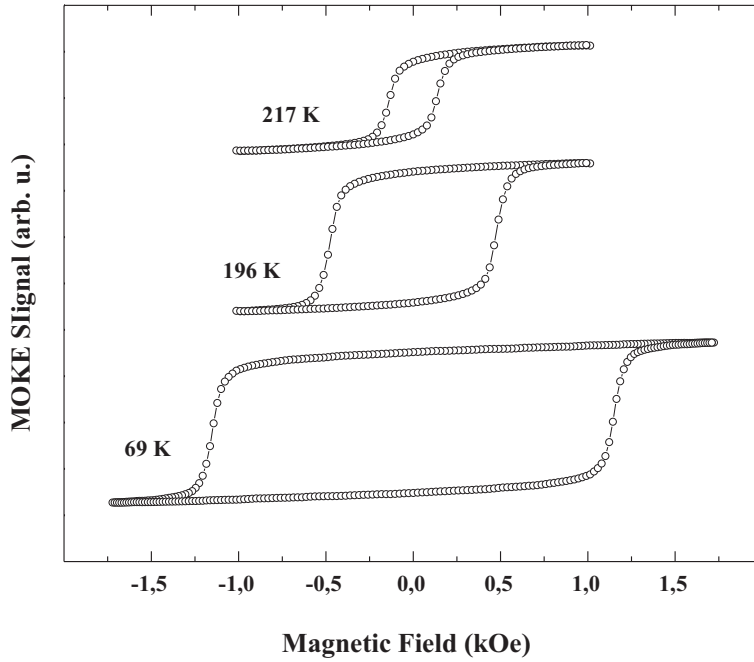


Figure 2.4. Tb hysteresis of 10-nm Tb on W(110) along the b -direction at different temperatures. After deposition of the Tb film at room temperature, the sample was annealed at 890 K. The temperature is kept constant by a computer-controlled regulator. For temperature errors see Appendix.

moments from an easy-axis of magnetization – the b -direction of the hcp lattice – to the neighboring hard-axis (a -direction) – within the basal plane. Because of the huge basal-plane anisotropy – at temperatures well below the ordering temperature – the moments can be assumed to lie strictly within the basal plane and the forces opposing the rotation arise from the crystalline anisotropy k_6^6 and from magnetostriction. The crystalline anisotropy is small throughout the temperature range of long-range order as compared to the magnetostriction, of which the contribution is expected to dominate the observed coercive fields. In Ref. [51] the coercive field is attributed to the effective (observable) anisotropy given by $g\mu_B J\sigma H_C = 36 |K_6^6(T)|$, with σ being the reduced magnetization. Within this picture the coercive field of 1.2 kOe (Fig. 2.4) at 69 K reveals a substantial K_6^6 anisotropy in the Tb film, and the slope at zero field indicates that there is a non-vanishing susceptibility even at low temperatures. (Note, that up to now there have been no data available on magnetization reversal in Tb metal.)

2.4.2 Magnetic anisotropy

In the absence of external magnetic fields the magnetization of a crystalline sample tends to be oriented along certain crystal axis which depend on the symmetry of the crystal. This so-called *the magnetic crystalline anisotropy* [69, 75] is due to the single-ion coupling of the spins to the crystal field [66, 76, 77]. The Hamiltonian of the magnetic anisotropy in an hcp crystal can be written as

$$H = K_2 Y_2^0(\theta) + K_4 Y_4^0(\theta) + K_6 Y_6^0(\theta) + K_6^6 \sin^6 \theta \cos 6\psi, \quad (2.33)$$

where K_i ($i = 2, 4, 6$) are the constants with a c -axis component and K_6^6 describes the

sixfold symmetry anisotropy within the hcp basal plane; the Y_i^0 ($i = 2, 4, 6$) are spherical harmonics. Experimental values of the anisotropy constants K_2 , K_4 , and K_6^6 for Gd and Tb are summarized in Table 2.1 (Ref. [55]).

	Gd	Tb
K_2	-0.3 ± 0.07	130 ± 25
K_4	0.15 ± 0.04	10.5 ± 2.8
K_6^6	-0.0015	0.42 ± 0.04

Table 2.1. Extrapolated zero temperature values (in K/atom) of the parameters K_2 , K_4 , K_6^6 deduced from experimental data.

According to Maxwell's law $\nabla B = 0$ a magnetized sample gives rise to a stray field outside its borders. The stray field energy strongly depends on the shape of the sample, giving rise to the so-called *shape anisotropy*. In thin film research where the sample thickness is much smaller than its lateral dimensions the shape anisotropy contribution becomes important giving rise to, e.g. transitions from in-plane to out-of-plane magnetization [78, 79].

2.4.3 Magnetic domains

In finite magnetic systems the coexistence of *exchange*, *stray-field*, and *anisotropy* contributions to the total energy leads to the formation of magnetic domains [80]. Within such a magnetic domain the magnetization is unidirectional. Domains with different directions of magnetization are separated by *domain walls* where the magnetization rotates from one direction to another.

The domain-wall *energy* and domain-wall *thickness* are proportional to $\sqrt{A \cdot K}$ and $\sqrt{A/K}$, respectively, where A is the exchange constant and K the relevant anisotropy constant [69, 75]. This means that in systems with large crystalline anisotropy the directions of the magnetic moments within the domain wall are orientated such that the hard directions are avoided in order to minimize the energy.

Due to the huge in-plane anisotropy in Tb metal (see subsection 2.4.2) it is energetically unfavorable to rotate the spins out of the basal plane. Therefore it is not surprising that in Tb the domain walls are perpendicular to the c -axis (and propagate along the c -axis), i.e. the rotation direction of the magnetic moments is comparable to the helical structure in the anti-ferromagnetic phase [81–83].

The domain structure in the Tb metal samples has been imaged earlier by decoration of the sample surface (stray field pattern) with iron particles (Bilster method). This is quite a crude procedure unsuitable for *in-situ* prepared thin film samples, which nowadays are investigated by scanning probe methods like atomic force microscopy (AFM), scanning force microscopy (SFM), scanning near-field optical microscopy (SNOM), and with spin-polarized STM [84].

2.4.4 Magnetostriction

Magnetostriction is the phenomenon of lattice deformation (described by the volume contraction ΔV) which arises from changes in magnetization (ΔM) and vice versa. The

magnetostriction in rare-earth metals is extremely large and contributes substantially (as an 'anomaly') to the thermal expansion [85, 86]. The 1st order phase transition from AF to FM is often accompanied by abrupt changes in the lattice constants [87, 88].

According to the *first law* of thermodynamics the energy in an isolated system is conserved. If the system is magnetic, any small increase of the energy can be written as

$$dE = dE_0 + dE_m, \quad (2.34)$$

where E_m and E_0 denote the magnetic and non-magnetic contributions, respectively. The magnetic energy is given by the integral of the magnetic induction B , produced by all currents and extended over all space, :

$$E_m = \frac{1}{2\mu_0} \int B^2 dV. \quad (2.35)$$

It includes the magnetization M and the external field H by $B = \mu_0(H + M)$. Considering only the sample, the integration limit is given by the border of the sample

$$E_m = \frac{1}{2\mu_0} B^2 V_{sample}. \quad (2.36)$$

In the following the volume is always considered as being the sample volume and therefore the index shall be omitted. Changes in $E_m(M, H, V)$ are obtained by the total differential with respect to the proper variables

$$\begin{aligned} dE_m &= \left(\frac{\partial E_m}{\partial H} \right)_{M,V} dH + \left(\frac{\partial E_m}{\partial M} \right)_{H,V} dM + \left(\frac{\partial E_m}{\partial V} \right)_{M,H} dV \\ &= \mu_0(H + M)V(dH + dM) + \frac{\mu_0}{2}(H + M)^2 dV. \end{aligned} \quad (2.37)$$

The non-magnetic contribution is the exchange of work and heat, i.e. $dE_0 = dA + dQ$ where $dQ = TdS$ and $dA = -PdV$. (Note that in a solid P is equivalent to a uniform tension σ).

Suppose changes in the system take place at a fixed temperature and without external work, then the appropriate thermodynamic potential is the free energy with the equilibrium condition $F = \text{minimum}$. For small changes in F one obtains

$$\begin{aligned} dF &= dE - d(TS) \\ &= -SdT + \left[\frac{\mu_0}{2}(H + M)^2 - P \right] dV + \mu_0(H + M)V(dH + dM). \end{aligned} \quad (2.38)$$

At thermal equilibrium ($dT = 0$), constant field ($dH = 0$), and with the condition $dF = 0$, one obtains an expression relating changes in the volume to changes in the magnetization

$$\frac{dV}{V} = \frac{\mu_0 dM}{\frac{P}{(H+M)} - \frac{1}{2}\mu_0(H + M)}. \quad (2.39)$$

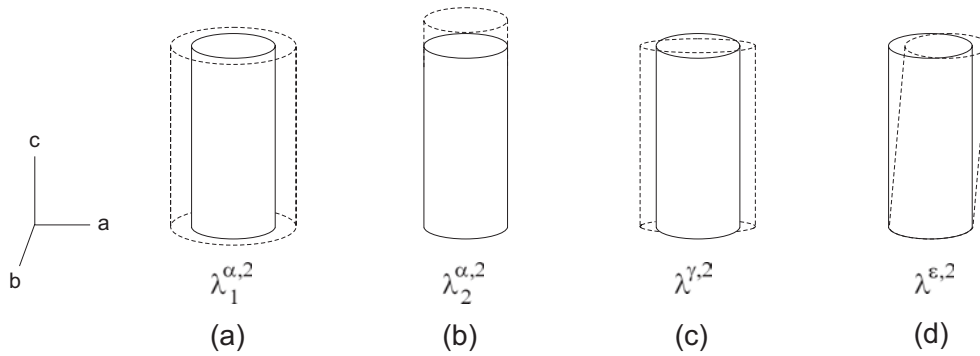


Figure 2.5. Magnetostriction modes in second order for hexagonal symmetry (from Clark et al., 1963).

Equation 2.39 gives the following a priori insight into the properties of magnetostriction: Changes in the magnetization are accompanied by changes in the volume, where the prefactor contains the pressure and the magnetic field as free parameters.

In lanthanide metals the magneto-elastic coupling between moments and lattice strain have profound consequences for the magnetization. Neglecting the anisotropy, the internal energy is the sum of the elastic (E_{el}) and the magnetoelastic (E_{me}) energy, which have a different dependence on the lattice strain ϵ . The magneto-elastic energy, $E_{me} \propto \epsilon$, is compensated by the elastic energy, $E_{el} \propto \epsilon^2$ [51], and the total energy is minimized at an equilibrium strain ϵ_0 – the *magnetostriction*. Because of their moderate elastic constants (the Young moduli are about five times weaker as compared to iron [89]) and the large orbital contribute to their $4f$ moments, the lanthanide metals display the largest known magnetostrictions on the order of 1% [51]. The only exception is Gd metal with its half-filled $4f$ shell. Magnetostrictive effects in Gd are typically two orders of magnitude smaller [7] and they contribute much less to the thermal lattice expansion than in Tb metal, where magnetostrictive and phonon parts are of comparable size [88, 90].

The *ordinary* magnetostriction is based on the *single-ion* mechanism (e.g. anisotropy), which originates from the interaction of the $4f$ moments with the crystal field. The *forced* magnetostriction and *anomalous thermal expansion*, by contrast, arise from the *two-ion* interaction between different lattice sites.

In the original formulation of Callen & Callen 1965 [76, 77] the theory of magnetostriction refers to the fully symmetric representation, where indices α, β, γ are commonly used to describe different strain modes of magnetostriction. Regarding both, one- and two-ion contributions, the magnetostriction $\Delta l/l$ in hexagonal symmetry is given by the expression (correct to second order [7])

$$\begin{aligned} \frac{\Delta l}{l} = & \left[\lambda_1^{\alpha,0} + \lambda_1^{\alpha,2} (\alpha_z^2 - 1/3) \right] (\beta_x^2 + \beta_y^2) \\ & + \left[\lambda_2^{\alpha,0} + \lambda_2^{\alpha,2} (\alpha_z^2 - 1/3) \right] \beta_z^2 \\ & + 1/2 \lambda^{\gamma,2} \left[(\alpha_x \beta_x + \alpha_y \beta_y)^2 - (\alpha_x \beta_y - \alpha_y \beta_x)^2 \right] \end{aligned}$$

$$+2\lambda^{\epsilon,2}(\alpha_x\beta_x + \alpha_y\beta_y)\alpha_z\beta_z. \quad (2.40)$$

The six magnetostriction constants λ are the experimentally determined quantities. Their explicit expressions contain elastic constants, and one- and two-ion magneto-elastic coefficients [76, 89]. The fully symmetric magnetostriction constants $\lambda_1^{\alpha,0}$ and $\lambda_1^{\alpha,2}$ contain only two-ion coefficients and are related to the anomalous thermal expansion (or exchange magnetostriction). The quantities α_i and β_i are direction cosines of the magnetization and strain directions, respectively. The α modes are symmetry-preserving dilatations in the basal plane ($\lambda_1^{\alpha,2}$) and along the c axis ($\lambda_2^{\alpha,2}$), the γ mode is a distortion of the hexagonal into orthorhombic symmetry (shearing of the basal plane), and the ϵ mode is a c -axis shear (Fig. 2.5).

In rare-earth metals with helical spin structures one observes a giant c -axis expansion anomaly of exchange origin [7, 90], which has an α -type character and is decisive for the *interlayer* coupling which has been calculated by Evenson and Liu [91]. Phenomenologically this exchange magnetostriction may be formulated in a molecular-field approximation as

$$\frac{\Delta l}{l} = \frac{cM^2}{Y} \left[\frac{\partial J_1}{\partial c} \cos \theta + \frac{\partial J_2}{\partial c} \cos 2\theta + \dots \right], \quad (2.41)$$

where J_1, J_2 are effective Fourier coefficients of the exchange energy between nearest neighbor (J_1) and next-nearest neighbor (J_2) layers. θ denotes the interplanar helical turn angle (the rotation angle between ferromagnetically ordered layers), c the lattice parameter, Y the Young modulus, and M the magnetization, with all these entities depending on the temperature T [7, 92]. In practice the temperature dependence of the observed dilatation is dominated by M^2 with the [...] factor in Eq. 2.41 providing small corrections [7].

On the basis of a classical single-ion model, the temperature dependence of the l -order magnetostriction constant $\lambda^{i,l}$ ($i = \alpha, \beta, \gamma$) is given by

$$\lambda^{i,l}(T) = \lambda^{i,l}(0) \hat{I}_{l+1/2}[\mathcal{L}^{-1}(\sigma)], \quad (2.42)$$

where $\hat{I}_{l+1/2}(X)$ is a normalized hyperbolic Bessel function, \mathcal{L}^{-1} the inverse of the Langevin function, and $\sigma = M(T)/M(0)$ is the reduced magnetization [89].

The a -, or b -axis strains are of the γ type (shearing of the basal-plane) and influence mainly the *intralayer* coupling. Using the notation of Callen & Callen [76, 77] the expression for the strains accompanying a rotation of the magnetization by an angle θ within the basal plane is given in lowest order by

$$\left. \frac{\Delta l}{l} \right|_{a,b} = \pm \lambda^{\gamma,2} \sin^2 \theta, \quad (2.43)$$

where $\theta = 0$ refers to the b -axis.

